

Wasserstein Geometry of Information Loss in Nonlinear Dynamical Systems

Yiting Duan^{1,3}, Zhikun Zhang², and Yi Guo^{*3}

¹Translational Health Research Institute, Western Sydney University, Australia

²School of Mathematics and Statistics, Northwestern Polytechnical University, Xi'an, China

³Centre for Research in Mathematics and Data Science, Western Sydney University, Australia

Abstract

Time-delay embedding is a powerful technique for reconstructing the state space of nonlinear time series. However, the fidelity of reconstruction relies on the assumption that the time-delay map is an embedding, which is implicitly justified by Takens' embedding theorem but rarely scrutinised in practice. In this work, we argue that time-delay reconstruction is not always an embedding, and that the non-injectivity of the time-delay map induced by a given measurement function causes irreducible information loss, degrading downstream model performance. Our analysis reveals that this local self-overlap stems from inherent dynamical properties, governed by the competition between the dynamical and the curvature penalty, and the irreducible information loss scales with the product of the geometric separation and the probability mass. We establish a measure-theoretic framework that lifts the dynamics to the space of probability measures, where the multi-valued evolution induced by the non-injectivity is quantified by how far the n -step conditional kernel $K^n(x, \cdot)$ deviates from a Dirac mass and introduce intrinsic stochasticity \mathcal{E}_n^* , an almost-everywhere, data-driven certificate of deterministic closure, to quantify irreducible information loss without any prior information. We demonstrate that \mathcal{E}_n^* improves reconstruction quality and downstream model performance on both synthetic and real-world nonlinear data sets.

Keywords: time-delay embedding, Takens' embedding theorem, information loss, nonlinear time-series analysis, dynamical system, differential topology

1 Introduction

Reconstructing nonlinear dynamics from partially observed trajectories via time-delay embedding has a rich history for signal processing and data-driven modelling [39, 8, 20, 24, 11, 9, 28, 12, 22] and has been widely used in nonlinear time-series tasks, including forecasting, causal detection, and equation discovery [42, 43, 4, 45, 51, 17]. However, these pipelines are built on a rarely verified assumption: the time-delay map is an embedding, or equivalently, injective on the relevant invariant set, where the induced evolution is single-valued and admits a deterministic closure. This discrepancy arises from

*Corresponding author: yg@westernsydney.edu.au

a misalignment between the generic guarantees of Takens’ embedding theorem and the practical constraints of finite, sparse samplings of certain measurement functions. Under certain conditions [47, 40], Takens’ theorem guarantees that a generic observation function yields a smooth embedding (i.e. continuous injective function) from the underlying state space to the reconstructed space. However, this guarantee is asymptotic and existential; for real-world time-series collected from given measurement functions, the injectivity need not hold. When it fails, the non-injectivity leads to irreducible information loss, degrading downstream model performance. Although it is possible to analyse the embedding map when the system equation is available [30, 31], it remains an open challenge to propose a certificate of deterministic closure in the data-driven settings. The central goal of this work is to establish a framework to investigate the mechanism of this non-injectivity, propose a data-driven certificate to quantify the induced information loss, and show its impact on downstream tasks.

For example, Convergence Cross Mapping (CCM), which is proposed by Sugihara *et al.* [45] and relies on the time-delay reconstruction, has been widely used in causal discovery for natural time-series. Figure 1 illustrates that when the time-delay reconstruction is not equally informative for the two observables, CCM can yield asymmetric cross-map skill and thereby mislead causal interpretation. Further downstream impacts are presented in Section 3.6.

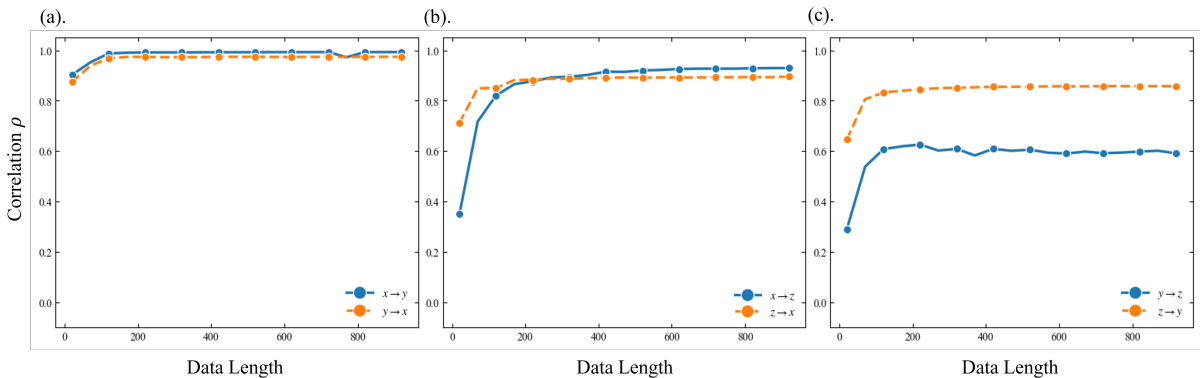


Figure 1: Performance of CCM on the Rössler system with dynamically-coupling state variables, where CCM results should yield high cross-map scores in both directions in terms of sufficiently informative time-delay reconstructions. Each panel reports the cross-map correlation ρ as a function of data length. (a). $X \Leftrightarrow Z$: both directions rapidly converge to a plateau near 1. (b). $X \Leftrightarrow Z$: both directions converge more slowly but still reach a higher plateau. (c). $Y \Leftrightarrow Z$: cross-map skill is asymmetric $Z \rightarrow Y$ high, $Y \rightarrow Z$ low, indicating that the chosen time-delay reconstruction is not equally informative for both variables, as an informative loss.

Considerable effort has been devoted to understanding the approximation error for time-delay reconstruction associated with certain downstream models [18, 27, 14], particularly regarding the asymptotic behavior of finite dimensional truncations that generate the information loss. Although these discussions build a solid foundation for numerical analysis, none verify whether the generic conditions are satisfied for a given measurement function. Furthermore, when the measurement function takes the form of a coordinate projection, the properties of the time-delay map are determined entirely by the inherent properties of the dynamical system. Because of the nonlinearity, the discrepancy of reconstruction

ability in the sense of non-injectivity between different dynamical variables is naturally generated, and this informative difference is closely correlated with signal characteristics in other fields [35, 34, 7].

Several efforts have been made to investigate the quality of the time-delay reconstruction induced by coordinate projection, for example, classical nonlinear observability is framed in differential geometry via the rank conditions on Lie derivatives [21, 2], however, it is not data-driven, which requires either analytic governing equations or stable Jacobian/derivative estimation. While other methods, such as SVDO [1] and DDA [19], are heuristic diagnostics but do not provide rigorous topological certificates.

The difficulty of investigating the non-injectivity of the time-delay map is twofold. The first point is that when the reconstruction map is non-injective, the induced flow on the reconstructed space exhibits a singular set, which is not well-defined and equals the set where the determinant of the time-delay map vanishes. Thus, approximating this singular set is difficult even in the ambient space of the attractor manifold. Another key subtlety is that a data-driven certificate cannot reasonably be posed as pointwise injectivity on the entire invariant set due to the complex geometry of the attractor, which often admits fractal sets of zero Lebesgue measure that are topologically nontrivial.

However, dissipative systems typically admit an SRB (physical) invariant measure, for which long-time empirical statistics along typical trajectories converge [40, 16, 5, 6]. By the Birkhoff ergodic theorem, finite trajectory sampling naturally probes sets of full physical measure, which motivates a measure-theoretic notion of observability: we seek to certify deterministic closure and injectivity on the statistically relevant portion of the attractor with respect to its SRB measure, or more generally, the SRB mass of a small neighbourhood of the singular set. This perspective turns the embedding step from an art into an auditable component of scientific inference. From this measure-theoretic perspective, if the time-delay map is non-injective, a single observed state is associated with multiple pre-images in the latent space, forming a fibre, and distinct states within the same fibre would evolve to different futures. Thus, determinism is destroyed in the reconstructed space: the statistically correct closed evolution is not a single-valued map but a conditional law of futures, equivalently, an induced Markov transition kernel, which degenerates to a Dirac mass only in the absence of self-overlap.

In this work, we connect delay-coordinate reconstruction with optimal transport by lifting the induced dynamics to Wasserstein space as illustrated in figure 2. Through our measure-theoretic framework, we show that the non-injectivity of the time-delay map arises from a competition between dynamical stretching and observed curvature, which are inherently determined by the dynamical system and result in irreducible information loss for downstream models, which is characterized by the distribution of the geometric separation and probability mass. To quantify this deviation, we introduce Intrinsic Stochasticity \mathcal{E}_n^* defined as the minimal Wasserstein-1 discrepancy between the n -step induced kernel and its best deterministic approximation (i.e. the closest Dirac measure), which provides a closure certificate: on a set of full measure in the reconstructed space, the n -step evolution is uniquely determined, and the effective dynamics are deterministic at that horizon. Finally, we demonstrate the utility of \mathcal{E}_n^* , the impact of non-injectivity across different models, and show that it is possible to improve downstream model performance on real-world datasets.

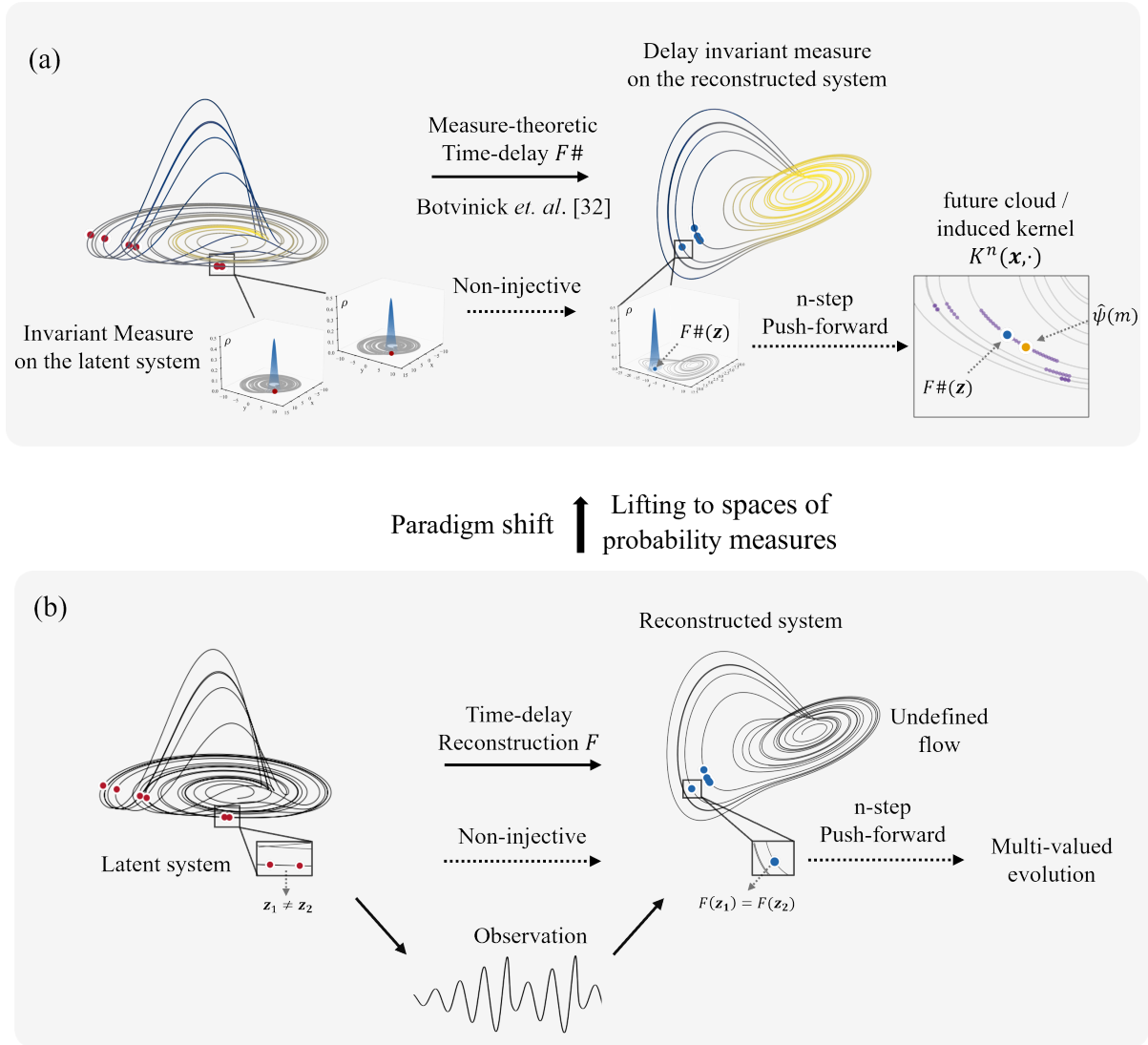


Figure 2: Overview of our measure-theoretic pipeline. (b) Illustrate the case when the time-delay map F is non-injective; it maps distinct latent states $\mathbf{z}_1 \neq \mathbf{z}_2$ to the same reconstructed state $\mathbf{x} = F(\mathbf{z}_1) = F(\mathbf{z}_2)$. Thus, a single-valued induced flow on the reconstructed space is not well-defined. (a) Describe the dual case after lifting to spaces of probability measures, where for each reconstructed state \mathbf{x} , the n -step fibre pushforward defines an induced kernel $K^{(n)}(\mathbf{x}, \cdot)$ (visualized as the purple future cloud). The non-injective point $F\#(\mathbf{z})$ induces a multi-modal/non-degenerate kernel while the intrinsic stochasticity \mathcal{E}_n^* quantifies the deviation of $K^{(n)}(\mathbf{x}, \cdot)$ from a Dirac mass by measuring the dispersion around the optimal predictor \hat{m} (the orange point).

2 Problem formulation and measure-theoretic lifting

This section introduces the dynamical and measure-theoretic setting used throughout the paper. Lifting dynamical systems to measure spaces is a typical technique in data-driven modelling; for example, the Perron-Frobenius operator provides a measure-theoretic linear operator of the dynamical system, which propagates the evolution of the probability distributions in time [10, 50, 6]. We focus on investigating the non-injectivity of the time-delay map in such measure space, and here we give a brief introduction to the related

work to establish a standard notation on which we build in Section 3.

2.1 Time delay embedding

Suppose we are in the following dynamical system:

$$\frac{d\mathbf{z}}{dt} = f(\mathbf{z}), \quad (1)$$

where $\mathbf{z} \in \mathcal{M}$, \mathcal{M} is a d -dimensional compact C^r manifold and denote the generated flow as $\{\Phi^t\}_{t \in \mathbb{R}}$ which admits an ergodic physical invariant probability measure ν , that captures the asymptotic statistical behaviour of long time trajectories. Typically, observations are measured at a fixed interval $\Delta t > 0$ by a measurement function $h(\mathbf{z}) \in \mathbb{R}^l$, and the induced discrete-time dynamical system is denoted as

$$T := \Phi^{\Delta t}. \quad (2)$$

In general, the choice of the measurement function is limited by practical constraints, and the dimensionality may also be smaller than d . In this work, we are primarily interested in the case of $l = 1$, and the measurement function is the coordinate projection of the dynamical variable (i.e. $h(z_1, z_2, z_3) = z_1$); in other words, we obtain a single one-dimensional time-series $\{y_k\}_{k \geq 0}$. We also discuss cases when $l > 1$ via multi-variate differential embeddings in the experiments section 3.4.

We have the following reconstruction of the latent dynamical system from the measurement using successive time delays as:

$$F : \mathcal{M} \rightarrow X \subseteq \mathbb{R}^m \quad (3)$$

is defined by

$$F(\mathbf{z}) = (h(\mathbf{z}), h(T^{-\tau}\mathbf{z}), \dots, h(T^{-(m-1)\tau}\mathbf{z}))^\top. \quad (4)$$

Here, we consider X as the reconstructed ambient space equipped with the Euclidean metric $d_X(\mathbf{x}, \mathbf{x}') = \|\mathbf{x} - \mathbf{x}'\|_2$, which contains the embedded image $F(\mathcal{M})$ on which the push-forward measure $\mu := F_{\#}\nu$ is supported. There are several benefits of this time-delay map, most notably that, given a hidden chaotic attractor, applying successive time delays with a suitable lag value τ yields a reconstruction of the hidden dynamical system which we can only partially observe. Takens' embedding theorem guarantees that for a generic observer h and a sufficiently large dimension, the map F is an embedding.

However, there is a sharp conflict between the ideal mathematical theorem and the physical constraints in practical use. The spirit of genericity in Takens' theorem means that the exceptional set of measurement functions which induce non-embedding time-delay maps is negligible in a topological sense (Baire category). Any inadequate candidate can be avoided by an arbitrarily small smooth perturbation, which is convenient for existence proofs, but limited in practical use when a fixed, given measurement function generates the dataset. For example, the exceptional set can be dense while still meagre, meanwhile the good set is generic.

Another important but often misinterpreted point is the embedding dimension. While Takens' theorem points out that the minimal dimension for achieving a time-delay embedding is at least $2m + 1$ ($m > 2d_A$ for the attractor manifold, where d_A denotes the box-counting dimension), this condition should not be interpreted as saying that simply stacking m successive time delays automatically provides m independent degrees

of freedom. For autonomous systems, successive time delays are always strongly correlated, especially when the lag value is small, the delay coordinate is redundant with a lower-dimensional reconstruction. On the other hand, when the time delay is too large, the reconstructed coordinates become decorrelated, and the time-delay vectors shape a degenerated, product-like geometry. An example is shown in figure 3. However, selecting delay parameters is nontrivial, and this remains an open problem: increasing m does not guarantee a successful embedding; at the same time, the choice of lag τ is crucial and determined by the mixing property of the latent system. As a result, when m is insufficient, or h is degenerate, F may fail to be injective, leading to self-overlap in reconstructed coordinates, that is, there exist distinct states $\mathbf{z}_1 \neq \mathbf{z}_2$ such that $F(\mathbf{z}_1) = F(\mathbf{z}_2)$.

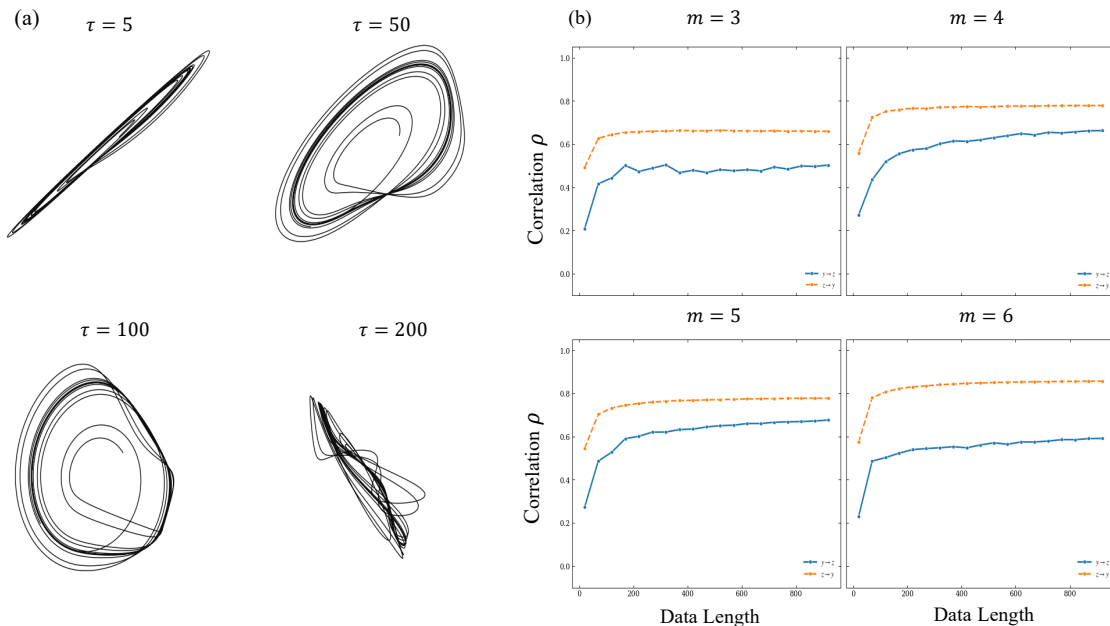


Figure 3: (a) The stretch-and-fold phenomenon as increasing the lag value τ for Rössler system using time-delay map induced by the z_1 -coordinate projection. (b). Using the same CCM example as in figure 1, increasing the embedding dimension for both z_1 and z_3 induced time-delay reconstruction from 3 to 6 does not eliminate the asymmetry in the cross-map skill for $Y \leftrightarrow Z$. In other words, the information loss does not diminish with larger m .

However, we emphasise that the non-injectivity of the time-delay map is inherently determined by the dynamical system, rather than by the delay parameter selection of the not well-defined time-delay map. We consider the well-defined differential embedding map where the small delay time takes the limit $\tau \rightarrow 0$:

$$F_h(\mathbf{z}) = \left(h(\mathbf{z}), \mathcal{L}_f h(\mathbf{z}), \dots, \mathcal{L}_f^{m-1} h(\mathbf{z}) \right), \quad (5)$$

where $\mathcal{L}_f h = \nabla h \cdot f$ is the Lie derivative, and it has been proved that the time-delay map is locally related to the time-delay map via a Taylor transform up to truncation [38]. A typical example is the Lorenz system; as proven by Cross *et al.* [13], no three-dimensional differential mapping can achieve a global diffeomorphism of the flow without self-overlap. More concrete examples of the Rössler system with different coordinate projections as

measurement functions can be found in Appendix A. Our goal is to quantify the ambiguity induced by such non-injectivity using only information available in the reconstructed space.

2.2 Measure-theoretic lifting and induced kernels

Here, we give the measure-theoretic form of time-delay embedding by lifting the dynamical system. The key point is that when the time-delay map is non-injective in the state space, the induced flow is not well-defined due to multiple-valued evolution; however, it yields a well-defined closed probability evolution on the Wasserstein space.

Given the dynamical system with an invariant measure ν on \mathcal{M} , let $\mu := F_{\#}\nu$ be the push-forward measure on X induced by ν . When F is non-injective, a reconstructed state \mathbf{x} does not correspond to a unique latent state; instead, it identifies a fibre:

$$F^{-1}(\mathbf{x}) = \{\mathbf{z} \in \mathcal{M} : F(\mathbf{z}) = \mathbf{x}\}, \quad (6)$$

which may contain multiple latent states compatible with the same reconstructed state \mathbf{x} , and therefore the evolution becomes to a conditional distribution of \mathbf{z} given \mathbf{x} . By the disintegration theorem [3], there exists a μ -almost everywhere, uniquely defined family of conditional probability measures $\{\nu_{\mathbf{x}}\}_{\mathbf{x} \in X}$ supported on the fibres $F^{-1}(\mathbf{x})$ such that, for any bounded measurable test function $\varphi : \mathcal{M} \rightarrow \mathbb{R}$, we have

$$\int_{\mathcal{M}} \varphi(\mathbf{z}) d\nu(\mathbf{z}) = \int_X \left(\int_{F^{-1}(\mathbf{x})} \varphi(\mathbf{z}) d\nu_{\mathbf{x}}(\mathbf{z}) \right) d\mu(\mathbf{x}). \quad (7)$$

Then, for any horizon $n \geq 1$, it is naturally to define the induced n -step transition kernel $K^n(\mathbf{x}, \cdot)$ on X as:

$$K^n(\mathbf{x}, \cdot) := (F \circ T^n)_{\#}\nu_{\mathbf{x}}. \quad (8)$$

Equivalently, for any bounded measurable $\psi : X \rightarrow \mathbb{R}$, we have

$$\int_X \psi(\mathbf{x}') K^n(\mathbf{x}, d\mathbf{x}') = \int_{F^{-1}(\mathbf{x})} \psi(F(T^n \mathbf{z})) d\nu_{\mathbf{x}}(\mathbf{z}). \quad (9)$$

The kernel $K^n(\mathbf{x}, \cdot)$ is the conditional probability distribution of the subsequent n -step reconstructions given the current reconstructed state.

If the delay-coordinate mapping is injective on a set of full ν -measure, then $\nu_{\mathbf{x}}$ is a Dirac mass for μ -a.e \mathbf{x} , and consequently $K^n(\mathbf{x}, \cdot)$ degenerates to a Dirac mass concentrated at the unique future reconstruction. Conversely, if F has self-overlap on a set of positive ν -measure, then $\nu_{\mathbf{x}}$ is typically nontrivial and $K^n(\mathbf{x}, \cdot)$ exhibits a spread that reflects ambiguity induced by non-injectivity. Section 3 quantifies this deviation from the deterministic limit by measuring how far $K^n(\mathbf{x}, \cdot)$ is from its closest Dirac mass, leading to the intrinsic stochasticity \mathcal{E}_n^* .

3 Intrinsic Stochasticity

Building on the measure-theoretic framework, we introduce the *intrinsic stochasticity* \mathcal{E}_n^* , a scalar optimal-transport metric that quantifies the non-injectivity of the time-delay map by measuring the deviation of $K^n(\mathbf{x}, \cdot)$ from deterministic evolution, and we next reveal the geometric mechanism that governs the generation of self-overlap and characterize the information loss.

3.1 Intrinsic Stochasticity

Definition 3.1 (Intrinsic Stochasticity). *For each $n \geq 1$, we define the minimal pointwise risk:*

$$m_n(\mathbf{x}) := \inf_{\mathbf{y} \in X} \ell_n(\mathbf{x}, \mathbf{y}), \quad (10)$$

and the Intrinsic Stochasticity:

$$\mathcal{E}_n^* := \int_X m_n(\mathbf{x}) \, d\mu(\mathbf{x}), \quad (11)$$

where the infimum is attained by the Fréchet/Geometric Median, denoted by $\Psi_n^*(\mathbf{x})$:

$$\Psi_n^*(\mathbf{x}) \in \arg \min_{\mathbf{y} \in X} \ell_n(\mathbf{x}, \mathbf{y}). \quad (12)$$

Functionally, \mathcal{E}_n^* quantifies the fundamental performance limitation of data-driven modelling subject to the information loss caused by self-overlap. The choice of the Geometric median $\Psi_n^*(\mathbf{x})$ over the conditional mean is preferred for chaotic systems. In the presence of self-overlap, the kernel $K^{(n)}(\mathbf{x}, \cdot)$ often becomes multimodal, e.g., splitting into two distinct branches. In this regime, the conditional mean that minimises the squared error may fall into the low-density region between branches, a physically invalid state. In contrast, the Geometric Median Ψ_n^* is robust to outliers and typically coincides with the dominant branch, thus a predictor with better physical meaning of chaotic systems.

Moreover, \mathcal{E}_n^* serves as a rigorous certificate for n -step deterministic closure. In the ideal limit where $\mathcal{E}_n^* = 0$, the conditional kernel degenerates to a Dirac mass almost everywhere, implying that the future state is uniquely determined by the current reconstruction, which generalizes Takens' condition by applying a continuous metric for quantifying the degree of determinism in the reconstructed space.

Generically, a vanishing n -step intrinsic stochasticity, $\mathcal{E}_n^* = 0$, implies that the time-delay map F is injective. However, if the system possesses symmetries that the observation function cannot distinguish, \mathcal{E}_n^* may vanish even if F is not injective. A classic example is the Lorenz63 system, which is invariant under the point symmetry $(z_1, z_2, z_3) \mapsto (-z_1, -z_2, z_3)$. Since the z_3 -coordinate observation is invariant under this transformation, the resulting time-delay reconstruction inherits this symmetry, thus becoming a two-to-one mapping that mods out the symmetry [15]. In this case, although the reconstruction achieves perfect deterministic closure and there is no information loss for the n -step evolution, this time-delay map itself remains topologically non-injective.

3.2 Geometric mechanism of information loss

We now elucidate the geometric mechanism that governs self-overlap. Our analysis reveals that \mathcal{E}_n^* is not an arbitrary numerical artefact stemming from parameter selection or measurement noise; instead, it is determined by a concrete physical competition between *dynamical stretching* and *observation curvature*, a mechanism inherent in the dynamical system, while the induced information loss scales with the product of the geometric separation and the probability mass.

3.2.1 Decomposition of folding

When the time-delay map F is non-injective, the conditional law $\nu_{\mathbf{x}}$ distributes latent states along a fibre $F^{-1}(\mathbf{x})$, whose geometry can be complex. Here, we focus our analysis

on the generic setting of *non-uniformly hyperbolic systems*. Specifically, we focus on *Pesin blocks* where the system admits an SRB measure with a local product structure. Thus, the conditional measure on an unstable leaf U_i is absolutely continuous with respect to the induced Riemannian volume $d\mathcal{V}_{U_i}(\mathbf{z})$, satisfying $d\nu|_{U_i}(\mathbf{z}) \asymp \rho^u(\mathbf{z}) d\mathcal{V}_{U_i}(\mathbf{z})$, where ρ^u is the bounded conditional SRB density along the unstable manifold, which describes how frequently the system naturally visits this state.

In this standard regularity setting, the conditional measure ν_x decomposes into a finite sum of atomic masses supported on distinct sheets, as:

$$\nu_{\mathbf{x}} = \sum_{i=1}^N p_i(\mathbf{x}) \delta_{\mathbf{z}_i(\mathbf{x})}, \quad (13)$$

which induces a *multimodal future evolution*. Pushing the measure forward by n steps, the transition kernel splits into discrete branches:

$$K^{(n)}(\mathbf{x}, \cdot) = \sum_{i=1}^N p_i(\mathbf{x}) \delta_{\mathbf{y}_i^{(n)}(\mathbf{x})}, \quad \text{where } \mathbf{y}_i^{(n)}(\mathbf{x}) := F(T^n \mathbf{z}_i(\mathbf{x})). \quad (14)$$

Now we restrict the reconstruction map on the i -th sheet U_i within the Pesin block R , denoted by $F_i := F|_{U_i \cap R}$. Since F_i is a diffeomorphism onto its image, applying the change of variables formula to the push-forward measure $\mu_i := (F_i)_\#(\nu|_{U_i \cap R})$, the Radon-Nikodym derivative of μ_i with respect to the Lebesgue measure on C is given by:

$$\frac{d\mu_i}{d\mathbf{x}}(\mathbf{x}) \asymp \frac{\rho^u(\mathbf{z}_i(\mathbf{x}))}{J_F(\mathbf{z}_i(\mathbf{x}))}, \quad \text{for } \mathbf{z} \in C, \quad (15)$$

where $\mathbf{z}_i(x) = F_i^{-1}(\mathbf{x})$ is the pre-image on the i -th sheet, and $J_F(\mathbf{z}) := \sqrt{\det(DF(\mathbf{z})DF(\mathbf{z})^\top)}$ is the coarea Jacobian of the time-delay map, which quantifies the local volume expansion or compression introduced by the reconstruction. Since $\mu|_C = \sum_{j=1}^N \mu_j$, the conditional probability of the i -th branch at \mathbf{x} is:

$$p_i(\mathbf{x}) = \frac{d\mu_i}{d\mu}(\mathbf{x}) = \frac{\frac{d\mu_i}{d\mathbf{x}}(\mathbf{x})}{\sum_{j=1}^N \frac{d\mu_j}{d\mathbf{x}}(\mathbf{x})} \asymp \frac{\rho^u(\mathbf{z}_i(\mathbf{x}))/J_F(\mathbf{z}_i(\mathbf{x}))}{\sum_{j=1}^N \rho^u(\mathbf{z}_j(\mathbf{x}))/J_F(\mathbf{z}_j(\mathbf{x}))}. \quad (16)$$

Defining the unnormalized weight $w_i(\mathbf{x}) := \rho^u(\mathbf{z}_i(\mathbf{x}))/J_F(\mathbf{z}_i(\mathbf{x}))$ yields a compact form as:

$$p_i(\mathbf{x}) = \frac{w_i(\mathbf{x})}{\sum_j w_j(\mathbf{x})}, \quad \text{where } w_i(\mathbf{x}) \asymp \frac{\rho^u(\mathbf{z}_i)}{J_F(\mathbf{z}_i)}. \quad (17)$$

Equation (17) implies that the probability weight of each outlier branch is determined by the ratio of visiting frequency (ρ^u) and the local geometric compression (J_F). The branch with higher probability weight means that the system visits frequently (high ρ^u) but is severely compressed by the time-delay map (low J_F). However, for these branches to manifest as irreducible ambiguity, they must be physically separated in the reconstructed space X . Furthermore, we show that the competition between dynamical stretching and the curvature penalty determines the extent to which branches drift apart.

3.2.2 Competition: Stretching vs. Curvature

To quantify the separation, we introduce the standard assumption of *Hyperbolic Visibility*, i.e., non-uniform hyperbolic expansion with rate λ_u and C^2 bounded observation, we first quantify the geometric separation $\Delta_n^-(\mathbf{x})$ between the dominant branch i_0 and the nearest competing outlier branch j .

The *effective expanded distance* r_n along the unstable manifold is defined as:

$$r_n(\mathbf{x}) := C_\epsilon^{-1} e^{n(\lambda_u - \epsilon)} \min_{j \neq i_0} d_u(\mathbf{z}_{i_0}, \mathbf{z}_j). \quad (18)$$

where λ_u is the positive Lyapunov exponent, ϵ is a small parameter fixing the non-uniformity, and C_ϵ is the associated Pesin constant. Denote the dominant pre-image as \mathbf{z}_{i_0} and \mathbf{z}_j be an outlier and define $\xi_{i_0} = T^n \mathbf{z}_{i_0}$ and $\xi_j = T^n \mathbf{z}_j$. A second-order Taylor expansion of F around ξ_{i_0} gives:

$$\delta_n = F(\xi_j) - F(\xi_{i_0}) = DF(\xi_{i_0})v_n + \frac{1}{2}v_n^\top \nabla^2 F(\xi_{i_0})v_n + O(\|v_n\|^3). \quad (19)$$

where $v_n = \xi_j - \xi_{i_0}$ is the difference vector on the latent manifold \mathcal{M} . Using the reverse triangle inequality, we obtain:

$$\|\delta_n\| \geq \|DFv_n\| - \frac{1}{2}\|\nabla^2 F\|\|v_n\|^2. \quad (20)$$

Since the dynamics is hyperbolic on the Pesin block, for sufficiently large n , the separation satisfies $\|v_n\| \geq r_n(\mathbf{x})$. The linear term is bounded below by the minimum expansion of the Jacobian, $\|DF(\xi_{i_0})v_n\| \geq \alpha_F \|v_n\|$, while the quadratic remainder is bounded by $K_{\text{Hess}}\|v_n\|^2$. Substituting these estimates into the Taylor expansion yields a mechanistic lower bound for the branch separation:

$$\Delta_n^-(\mathbf{x}) \geq \alpha_F r_n(\mathbf{x}) - \frac{K_{\text{Hess}}}{2} r_n(\mathbf{x})^2. \quad (21)$$

Here, α_F is the minimum singular value of the Jacobian of F along unstable directions, and K_{Hess} bounds the observation curvature.

This inequality arises from the two opposing geometric forces that determine the separation of outlier branches. The first term, $\alpha_F r_n(\mathbf{x})$, represents the dynamical force. The minimum expansion rate of F along unstable directions (α_F), amplified exponentially by the Lyapunov exponent λ_u , drives the states apart. This force attempts to resolve the ambiguity by separating the trajectories in X . The second term acts as a curvature penalty, imposing a geometric obstruction. The second-order curvature of the observation map ($K_{\text{Hess}} \geq |\nabla^2 F|$) acts as a folding force. Even if points are separated on the manifold, high curvature in the observation function can bend their images back into proximity in the ambient space, as mixing the branches.

We provide a numerical validation of this competition mechanism via the Rössler system in figure 4, where the measurement function is the z_1 -coordinate projection and we use the differential embedding $F := (z_1, \dot{z}_1, \ddot{z}_1)$ as the reconstruction map. Here the dynamical stretching proxy α_F is computed as the smallest singular value of the analytic Jacobian DF of F and the curvature penalty proxy κ is computed from the time derivative curvature $t \mapsto (z_1, \dot{z}_1, \ddot{z}_1)$ via $\kappa = |V \times A|/|V|^3$, where $V = (\dot{z}_1, \ddot{z}_1, \dddot{z}_1)$ and $A = (\ddot{z}_1, \dddot{z}_1, z_1^{(4)})$, where $z_1^{(4)}$ denotes the fourth-order Lie derivative of z_1 . The geometric mechanism is illustrated in two regions \mathcal{R}_1 and \mathcal{R}_2 . \mathcal{R}_1 exhibits a high dynamical stretching α_F with a high curvature penalty κ , resulting in less folding. However, \mathcal{R}_2 holds a lower α_F but a higher curvature penalty κ , thus yielding the folding region.

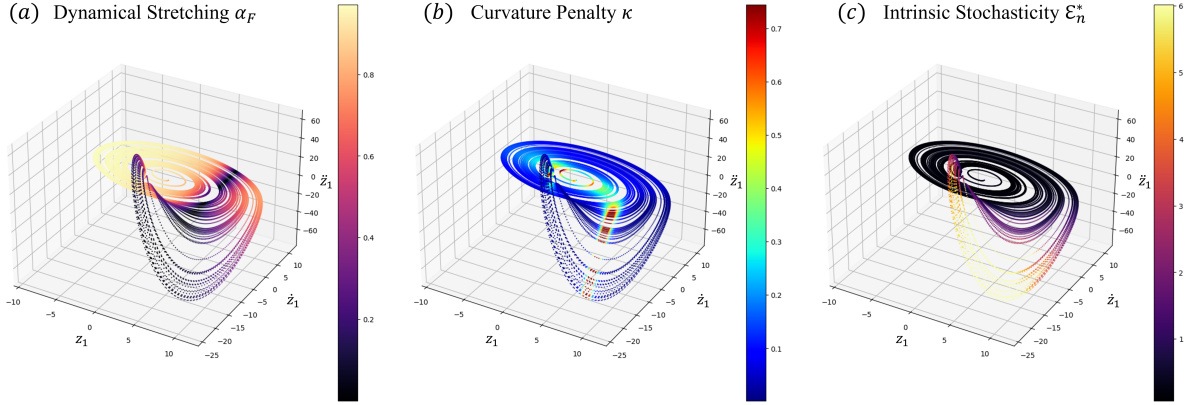


Figure 4: A numerical validation of the dynamical separation and observation curvature competition mechanism of the Rössler system under the differential embedding $F = (z_1, \dot{z}_1, \ddot{z}_1)$.

3.2.3 The Scaling Law of Information Loss

Combining the mass decomposition (Eq. 17) and the separation geometry (Eq. 21), we derive a unified physical law for intrinsic stochasticity \mathcal{E}_n^* . We present this as a geometric scaling relation that governs the magnitude of information loss. Denote the outlier mass as:

$$b_n(\mathbf{x}) := 1 - p_{i_0}(\mathbf{x}), \quad (22)$$

Then we obtain the scaling law:

$$\mathcal{E}_n^* \sim \int_A b_n(\mathbf{x}) \cdot \Delta_n(\mathbf{x}) d\mu(\mathbf{x}). \quad (23)$$

Here, $\Delta_n(\mathbf{x})$ is the *characteristic separation* between the dominant branch and the outliers. Since we provide a lower bound, the notation \sim for the upper part is justified by the definition of the geometric median. As a minimiser, it is inherently bounded above by the risk of the dominant branch, which also scales with the same geometric product, since in the local product structure, distances to different outlier sheets are of the same asymptotic order $\Delta_n \asymp \Delta_n^-$.

This relation identifies the specific mechanism: \mathcal{E}_n^* becomes significant only when two conditions are met simultaneously: (1) There is non-negligible probability mass on outlier branches ($b_n > 0$), and (2) The dynamics stretches these branches apart faster than the observation curvature folds them back ($\Delta_n > 0$). Hyperbolic stretching drives separation exponentially in n , while curvature introduces a quadratic correction that can partially suppress separation at small scales. This balance identifies a concrete competition mechanism between stretching and curvature that governs the intrinsic stochasticity. Furthermore, we validate this scaling law by providing upper and lower bounds on the tightness using the following example.

Figure 5 validates the SRB-weighted mass-separation lower bound and upper bound on the Rössler system using the differential embedding $F = (z_3, \dot{z}_3, \ddot{z}_3)$. For each base point $x = F(\mathbf{z}_t)$, we form a k -nearest neighbourhood in X with a Theiler window to avoid trivial temporal correlations, and push this neighbourhood forward by n -step to obtain an empirical sample of $K^{(n)}(\mathbf{x}, \cdot)$. We then compute the pointwise proxy $\widehat{m}_n^{(w)}(\mathbf{x})$ as the SRB-weighted Geometric median cost of this empirical kernel via a Weiszfeld iteration.

For the lower bound analysis, we restrict to a well-resolved subset A , where the pushed-forward cloud is genuinely bimodal, consisting of two nontrivial clusters with positive silhouette scores, and where the finite-time stretching is strong, as measured by a Pesin block proxy based on tangent-map growth. This subset comprises 110 of the 400 sampled base points. Using the 95% quantile of the branch-weight ratio $r = w_{\max}/w_2$ gives $r_*^{95} = 4.689$ and hence a folding-mass lower bound $b_0 = (1 + r_*^{95})^{-1} = 0.176$. On this subset we observe $P(\widehat{m}_n^{(w)} \geq b_0 \Delta) = 1.00$ with correlation $\rho_{\text{corr}} = 0.998$, and the tightness ratio $Q_{\text{LB}} := \widehat{m}_n^{(w)} / (b_0 \Delta)$ concentrates at an $O(1)$ constant. These results confirm that elevated intrinsic stochasticity occurs precisely when a non-negligible portion of probability mass is forced to travel across a dynamically generated inter-branch separation in the reconstructed space.

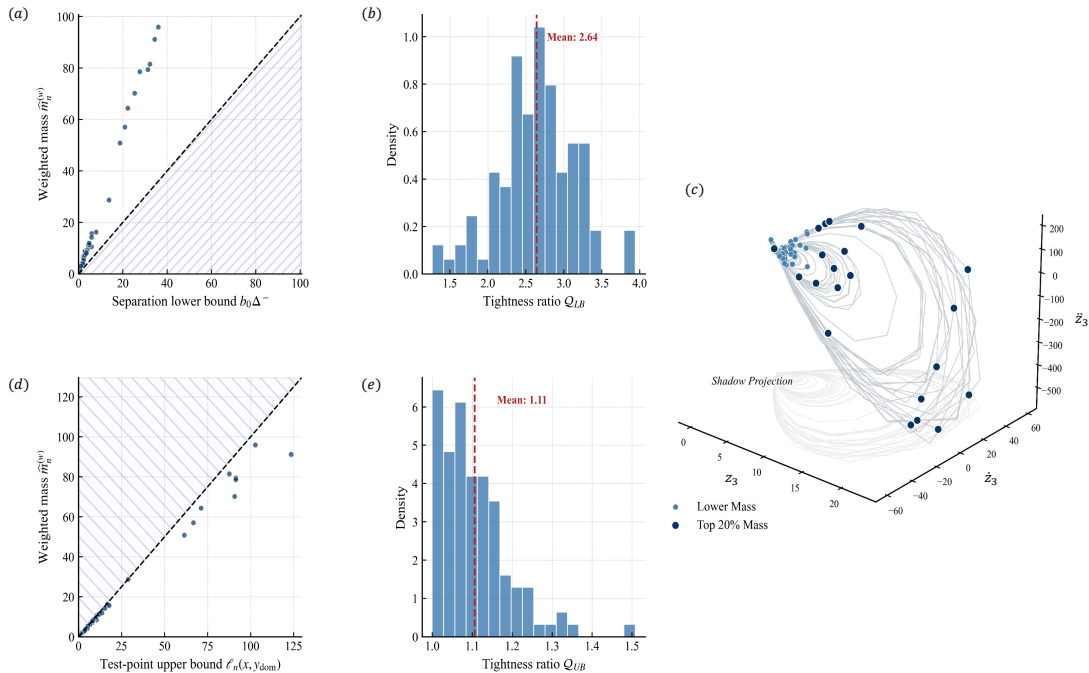


Figure 5: Numerical Verification of the lower and upper bound via Rössler system with differential mapping $F = (z_3, \dot{z}_3, \ddot{z}_3)$. (a). Separation lower bound $b_0 \Delta^-$. (b). Tightness ratio Q_{LB} . (c). Reconstructed system via differential mapping F and accepted query states are colored by the estimated $\widehat{m}_n^{(w)}$. Darker points indicate the top 20% largest $\widehat{m}_n^{(w)}$, i.e., locations with the strongest evidence of multi-valued evolution. In contrast, lighter points correspond to lower $\widehat{m}_n^{(w)}$, which yields a single-valued, Dirac-like push-forward kernel.

For the upper bound, we validate the test-point upper bound on the same Pesin-filtered sample used before. For each accepted base point $\mathbf{x} \in C$, we take the dominant-branch test point $\mathbf{y}_{\text{dom}}(\mathbf{x}) = \mathbf{y}_{i_0(\mathbf{x})}^{(n)}(\mathbf{x})$ as the predictor and evaluate the corresponding one-step cost

$$U_n(\mathbf{x}) = \ell_n(\mathbf{x}, \mathbf{y}_{\text{dom}}(\mathbf{x})) = \int_X d_X(\mathbf{y}_{\text{dom}}(\mathbf{x}), \mathbf{y}') K^{(n)}(\mathbf{x}, d\mathbf{y}'), \quad (24)$$

which satisfies $m_n(\mathbf{x}) \leq U_n(\mathbf{x})$ by definition of $m_n(\mathbf{x}) = \inf_{\mathbf{y}} \ell_n(\mathbf{x}, \mathbf{y})$. Figure 5 shows that this bound is not only valid within numerical precision but also quantitatively tight. The scatter plot reveals no systematic violations, and the tightness ratio $Q_{\text{UB}} := U_n(\mathbf{x}) / \widehat{m}_n^{(w)}(\mathbf{x})$ concentrates near unity, indicating that the dominant-branch test point provides a near-optimal deterministic prediction in the selected Pesin block regime, which complete the

lower-bound results by bracketing the intrinsic stochasticity scale within an $O(1)$ envelope on the same Pesin-filtered regime.

3.3 Estimator and algorithm

Let $\{\mathbf{x}_t\}_{t=0}^{T-1} \subset X$ denote reconstructed states and fix a horizon $n \geq 1$. For a query index $q \in \{0, \dots, T-n-1\}$, let $\mathcal{N}_k(q)$ be the set of indices of the k nearest neighbors of \mathbf{x}_q among $\{\mathbf{x}_t\}_{t=0}^{T-n-1}$ with a Theiler exclusion window to mitigate temporal correlations. Pushing the neighborhood forward by n -steps yields a cloud $\mathcal{Y}_q := \{\mathbf{y}_j\}_{j=1}^k := \{\mathbf{x}_{t+n} : t \in \mathcal{N}_k(q)\} \subset X$, which approximates the conditional kernel $K^{(n)}(\mathbf{x}_q, \cdot)$. Throughout this section, we use the uniform empirical kernel:

$$\widehat{K}^{(n)}(\mathbf{x}_q, \cdot) := \frac{1}{k} \sum_{j=1}^k \delta_{\mathbf{y}_j}. \quad (25)$$

Under mixing/ergodic and regularity assumptions, and for $k \rightarrow \infty$, $k/N \rightarrow 0$, the uniform KNN empirical measure $\widehat{K}^{(n)}(\mathbf{x}, \cdot)$ converges weakly to $K^n(\mathbf{x}, \cdot)$ for μ -a.e. \mathbf{x} [44].

Given $\widehat{K}^{(n)}(\mathbf{x}_q, \cdot)$, define the empirical pointwise risk

$$\widehat{\ell}_{n,k}(\mathbf{x}_q, \mathbf{y}) := \int_X d_X(\mathbf{y}, \mathbf{y}') \widehat{K}^{(n)}(\mathbf{x}_q, d\mathbf{y}') = \frac{1}{k} \sum_{j=1}^k d_X(\mathbf{y}, \mathbf{y}_j), \quad (26)$$

and the empirical Fréchet median cost

$$\widehat{m}_{n,k}(\mathbf{x}_q) := \min_{\mathbf{y} \in X} \widehat{\ell}_{n,k}(\mathbf{x}_q, \mathbf{y}) = \min_{\mathbf{y} \in X} \frac{1}{k} \sum_{j=1}^k d_X(\mathbf{y}, \mathbf{y}_j), \quad (27)$$

which we compute numerically using a Weiszfeld iteration. Finally, for a set of query indices \mathcal{Q} with $|\mathcal{Q}| = N_{\mathcal{Q}}$, we estimate

$$\widehat{\mathcal{E}}_{n,k}^* := \frac{1}{N_{\mathcal{Q}}} \sum_{q \in \mathcal{Q}} \widehat{m}_{n,k}(\mathbf{x}_q). \quad (28)$$

The proposed algorithm is outlined in Algorithm 1.

Algorithm 1 Estimating intrinsic stochasticity at fixed neighbourhood scale k

Require: Reconstructed states $\{\mathbf{x}_t\}_{t=0}^{T-1} \subset X$; horizon n ; neighborhood count k ; Theiler window w ; Number of queries $N_{\mathcal{Q}}$.

Ensure: $\widehat{\mathcal{E}}_{n,k}^*$.

- 1: Sample query indices $\mathcal{Q} \subset \{0, \dots, T-n-1\}$ uniformly at random with $|\mathcal{Q}| = N_{\mathcal{Q}}$.
 - 2: **for** $q \in \mathcal{Q}$ **do**
 - 3: Find $\mathcal{N}_k(q)$: the k -nearest neighborhood $\mathcal{N}_k(q)$ of \mathbf{x}_q with the Theiler window.
 - 4: Form $\mathcal{Y}_q := \{\mathbf{x}_{t+n} : t \in \mathcal{N}_k(q)\}$.
 - 5: Compute $\widehat{m}_{n,k}(\mathbf{x}_q) = \min_{\mathbf{y} \in X} \frac{1}{k} \sum_{\mathbf{y}_j \in \mathcal{Y}_q} d_X(\mathbf{y}, \mathbf{y}_j)$ via Weiszfeld iteration.
 - 6: **end for**
 - 7: **return** $\widehat{\mathcal{E}}_{n,k}^* = \frac{1}{N_{\mathcal{Q}}} \sum_{q \in \mathcal{Q}} \widehat{m}_{n,k}(\mathbf{x}_q)$.
-

3.4 \mathcal{E}_n^* applied to synthetic examples

In realistic scenarios, the properties of the measurement function significantly influence whether the time-delay map is injective. To investigate the intrinsic properties of dynamical systems, we focus on coordinate projections; e.g. the z_1 -coordinate projection is $F(z_1, z_2, z_3) = z_1$. We analyse the performance of our method using the synthetic Rössler system with various differential embeddings, including univariate differential embeddings (e.g. $F_{z_1} = (z_1, \dot{z}_1, \ddot{z}_1)$), linear combination of multiple observables (e.g. $F_{z'_1} = (z_2 + z_3, \dot{z}_2 + \dot{z}_3, \ddot{z}_2 + \ddot{z}_3)$), multi-variate differential embeddings except $F = (z_1, z_2, \dot{z}_2)$ and $F = (z_1, z_3, \dot{z}_3)$ due to rank deficiency. These embeddings have analytic forms, allowing us to explicitly determine whether the mapping is injective or a diffeomorphism. Analytic expressions for all differential embeddings are provided in Appendix A. For a fair comparison, the push-forward step is fixed at $p = 20$, with a sample size of $N = 5000$ and $k = 50$.

We compare the performance of our method against three established approaches: analytic observability indices [30], the False Nearest Neighbours (FNN) criterion [25], and the SVDO method [1]. The observability indices require the explicit analytic formulation of the embedding and assess local invertibility via the Jacobian rank. In contrast, SVDO is a data-driven approach relying on heuristic singular value thresholds. To enable a more direct assessment of non-injectivity, we adapt the classical FNN concept into a supervised metric, denoted as Fold_Frac (FF). Instead of using heuristic criteria, this modified FF directly compares the true states \mathbf{z}_t with the reconstructed states \mathbf{x}_t , and we classify a neighbour in the reconstruction space as false if the corresponding points are distant in the latent space.

For each query q , let $\mathcal{N}_k(q)$ denote the indices of the k nearest neighbours of x_q after applying the Theiler exclusion window [48]. We define the pairwise distance in the latent space as:

$$\Delta_{\mathbf{z}}(q, t) = \|\mathbf{z}_q - \mathbf{z}_t\|_2. \quad (29)$$

Using a tolerance threshold δ_{tol} , set to 5% of the attractor diameter, the metric is defined as the average fraction of false neighbours:

$$FF := \frac{1}{N_q} \sum_q \left[\frac{1}{k} \sum_{t \in \mathcal{N}_k(q)} \mathbf{1}_{\Delta_{\mathbf{z}}(q,t) > \delta_{\text{tol}}} \right]. \quad (30)$$

Ideally, a diffeomorphism yields a Fold_Frac of zero, with increasing values reflecting the severity of topological folding. To ensure consistency, the neighbour set $\mathcal{N}_k(q)$ used for the supervised Fold_Frac diagnosis is identical to that employed in the estimation of \mathcal{E}_n^* . The comparison results are shown in Table 1. Note that FF and analytic observability indices rely on information unavailable in real applications, so we treat them as diagnostics for synthetic validation only. Our estimator \mathcal{E}_n^* is data-driven and targets the degeneracy of the conditional future cloud, which directly quantifies practical closure at the neighbourhood scale implied by the data.

Multi-variate embeddings involving the z_3 -variable, such as (z_2, z_3, \dot{z}_2) and (z_1, z_3, \dot{z}_1) are diffeomorphisms and they are expected to provide a lower \mathcal{E}_n^* because of a global dynamical closure. In stark contrast, our estimator assigns substantially higher penalties to these embeddings. This apparent tension reflects the distinction between mathematical invertibility and finite-resolution predictability. While a diffeomorphism guarantees an exact coordinate change and hence injectivity, our estimator $\hat{\mathcal{E}}_{n,k}^*$ quantifies closure at a

Table 1: Comparison of intrinsic stochasticity \mathcal{E}_n^* (the lower the better), Observability index D (the higher the better), FF (the lower the better), and SVDO score (the higher, the better) for Rössler multi-variate differential embeddings. In the following cases, $(z_2, \dot{z}_2, \ddot{z}_2)$, (z_1, z_2, \dot{z}_1) , (z_1, z_3, \dot{z}_1) and (z_2, z_3, \dot{z}_2) are diffeomorphism, which admit an explicit analytic inverse.

Embedding	$\hat{\mathcal{E}}_{n,k}^*$ (data-driven)	D (analytic)	SVDO (data-driven)	FF (supervised)
$(z_2, \dot{z}_2, \ddot{z}_2)$	0.05 ± 0.00	0.14	0.18 ± 0.07	0.024
(z_1, z_2, \dot{z}_1)	0.05 ± 0.00	0.15	0.15 ± 0.05	0.024
$(z_1 + z_2, \dot{z}_1 + \dot{z}_2, \ddot{z}_1 + \ddot{z}_2)$	0.09 ± 0.00	0.05	0.19 ± 0.06	0.036
$(z_1, \dot{z}_1, \ddot{z}_1)$	0.11 ± 0.00	0.03	0.16 ± 0.03	0.037
$(z_2 + z_3, \dot{z}_2 + \dot{z}_3, \ddot{z}_2 + \ddot{z}_3)$	0.73 ± 0.03	0.01	0.10 ± 0.03	0.049
$(z_1 + z_3, \dot{z}_1 + \dot{z}_3, \ddot{z}_1 + \ddot{z}_3)$	1.88 ± 0.08	0.00	0.10 ± 0.02	0.062
(z_1, z_3, \dot{z}_1)	4.70 ± 0.17	0.15	0.11 ± 0.04	0.10
(z_2, z_3, \dot{z}_2)	4.71 ± 0.17	0.67	0.14 ± 0.04	0.10
(z_2, z_3, \dot{z}_3)	12.11 ± 0.39	0.01	0.18 ± 0.03	0.12
$(z_3, \dot{z}_3, \ddot{z}_3)$	14.37 ± 0.44	0.00	0.07 ± 0.01	0.089

finite spatial scale determined by the data-driven neighbourhood used to approximate the conditional kernel $K^n(\mathbf{x}, \cdot)$. In particular, at fixed neighbourhood count k with Theiler exclusion, $\hat{\mathcal{E}}_{n,k}^*$ depends not only on whether F is injective, but also on the effective neighbourhood radius required to collect k admissible neighbours. Consequently, a reconstruction can be analytically invertible yet still yield a large $\hat{\mathcal{E}}_{n,k}^*$ when the estimator is forced to operate at a non-negligible resolution.

To make this mechanism explicit, for each \mathbf{x}_q we record the k th-neighbour distance after the Theiler window:

$$r_k(\mathbf{x}_q) := \max_{t \in \mathcal{N}_k(q)} \|\mathbf{x}_t - \mathbf{x}_q\|_2, \quad (31)$$

and summarize its distribution by the median $\tilde{r}_k := \text{median}_{q \in \mathcal{Q}} r_k(\mathbf{x}_q)$ and the upper-tail statistic $\tilde{r}_{k,0.9} := \text{quantile}_{0.9}(r_k(\mathbf{x}_q))$. Results are listed in the table 2. These diagnostics reveal that the poor performance of embeddings such as (z_2, z_3, \dot{z}_2) is not driven by a large typical radius, the medians are comparable to those of the best embeddings, but by an elevated tail: a nontrivial fraction of queries require much larger neighborhoods to satisfy the Theiler constraint and reach k neighborhoods. Since the push-forward cloud is evaluated over a fixed horizon n , these rare but large-radius neighbourhoods undergo substantially stronger finite-time divergence and contribute disproportionately to the average Fréchet-median cost, thereby inflating $\hat{\mathcal{E}}_{n,k}^*$.

This behaviour is intrinsically linked to the dynamical role of the z_3 -variable in the Rössler system. The z_3 -component remains close to zero for long intervals, punctuated by intermittent spikes where the flow exhibits intense stretching and twisting. Reconstructions that explicitly include z_3 or its derivatives inherit a form of phase ambiguity at finite resolution: points that are close in the Euclidean embedding metric may lie at markedly different phases relative to an impending spike [29]. Such small geometric discrepancies are rapidly amplified under forward propagation, keeping the conditional future cloud $K^n(\mathbf{x}, \cdot)$ broad at the practical neighbourhood scales implied by the data. The radius diagnosis $(\tilde{r}_k, r_{k,0.9})$ supports this interpretation: even when the mapping is globally invertible, the estimator must sometimes operate at large effective radii, at which chaotic divergence

Table 2: Effective neighbourhood radius diagnostics after Theiler exclusion. We report the median \tilde{r}_k and the 90% quantile $r_{k,0.9}$ of the k th-neighbour distance $r_k(\mathbf{x}_q)$ over query points.

Embedding	\tilde{r}_k (median)	$\tilde{r}_{k,0.9}$ (90%)
$(z_2, \dot{z}_2, \ddot{z}_2)$	0.07	0.17
(z_1, z_2, \dot{z}_2)	0.07	0.17
$(z_1 + z_2, \dot{z}_1 + \dot{z}_2, \ddot{z}_1 + \ddot{z}_2)$	0.06	0.18
$(z_1, \dot{z}_1, \ddot{z}_1)$	0.07	0.19
$(z_2 + z_3, \dot{z}_2 + \dot{z}_3, \ddot{z}_2 + \ddot{z}_3)$	0.06	0.39
$(z_1 + z_3, \dot{z}_1 + \dot{z}_3, \ddot{z}_1 + \ddot{z}_3)$	0.06	0.68
(z_1, z_3, \dot{z}_1)	0.06	0.91
(z_2, z_3, \dot{z}_2)	0.07	0.93
(z_2, z_3, \dot{z}_3)	0.08	7.91
$(z_3, \dot{z}_3, \ddot{z}_3)$	0.07	16.84

dominates the finite-sample closure score.

3.5 \mathcal{E}_n^* applied to real datasets

Here, we apply \mathcal{E}_n^* to two real-world time-series open datasets, the trajectory of a double pendulum [23, 22], and the measles outbreak data [36]. Similar to the Rössler example, we find that the value of \mathcal{E}_n^* can represent the quality of embedding, the proportion of injectivity.

Double Pendulum: We first consider the measurements of a double pendulum, which contains two datasets: the synthetic data and the measurement data. The Lagrangian can be written as:

$$\mathcal{L} = \frac{1}{2}(m_1(\dot{x}_1^2 + \dot{y}_1^2) + m_2(\dot{x}_2^2 + \dot{y}_2^2)) + \frac{1}{2}(I_1\dot{\theta}_1^2 + I_2\dot{\theta}_2^2) - (m_1y_1 + m_2y_2)g, \quad (32)$$

where $x_1 = a_1 \sin(\theta_1)$, $x_2 = l_1 \sin(\theta_1) + a_2 \sin(\theta_2)$, $y_1 = a_1 \cos(\theta_1)$ and $y_2 = l_1 \cos(\theta_1) + a_2 \cos(\theta_2)$, θ_1 and θ_2 are the angles between the top and bottom pendulum and the vertical axis, m_1 and m_2 are the masses spread over each arm, l_1 and l_2 are the lengths, a_1 and a_2 are the distances from the joints to the centre of the masses of each arm, and I_1 and I_2 are the moments of inertia for each arm. Using the Euler-Lagrange equations, we can construct two second-order differential equations for this chaotic system:

$$\frac{d}{dt} \left(\frac{\partial \mathcal{L}}{\partial \dot{\theta}_i} \right) - \frac{\partial \mathcal{L}}{\partial \theta_i} = 0, \quad i = 1, 2. \quad (33)$$

The data are sampled at $\Delta t = 0.001$ s for both the simulated and the experimental datasets.

Similarly, we can write down the expression for the differential embedding of this four-dimensional dynamical system. Instead of calculating and comparing these differential embeddings one by one, we compare the following types of differential embeddings built from the same measured angle:

$$\begin{aligned} F_{\theta_i} &= (\theta_i, \dot{\theta}_i, \ddot{\theta}_i, \ddot{\theta}_i) \\ F_{\sin \theta_i} &= (\sin \theta_i, \dot{\sin \theta}_i, \ddot{\sin \theta}_i, \ddot{\sin \theta}_i) \end{aligned} \quad (34)$$

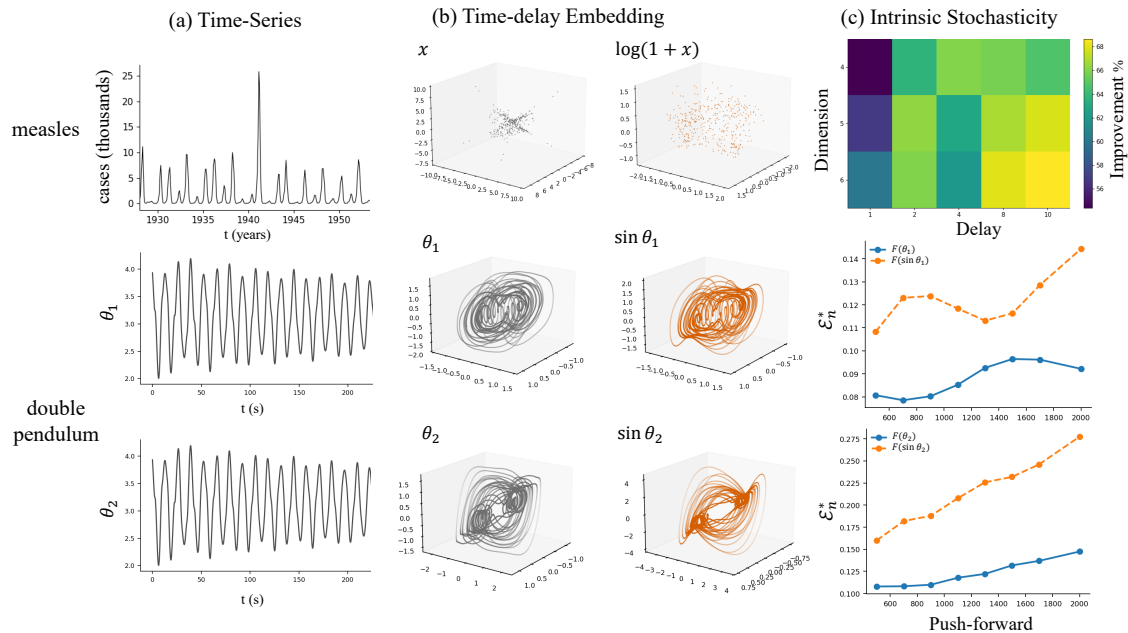


Figure 6: Application of Intrinsic Stochasticity for two real-world systems: a measles outbreak and an experimental double pendulum dataset. (a). Row time-series. (b). Reconstructed attractor manifold. For measles data, we consider time-delay embeddings over a grid of time-delay embedding parameters (m, τ) and visualise the reconstructions after PCA (first three components) for the raw counts \mathbf{x} and the log-transformed signal $\log(1 + \mathbf{x})$. For the double pendulum, we reconstruct using the differential embedding maps $F(\cdot)$ in (34) for the measured angles θ_1 and θ_2 , and display the first three coordinates of $F(\theta_1)$ and $F(\sin \theta_i)$. (c). Quantitative intrinsic stochasticity. For measles we report the percentage reduction: $\text{Improvement}(\%) = (\hat{\mathcal{E}}_{n,k}^*(\mathbf{x}) - \hat{\mathcal{E}}_{n,k}^*(\log(1 + \mathbf{x}))) / \hat{\mathcal{E}}_{n,k}^*(\mathbf{x})$, computed with $k = 50$ for KNN, showing the consistent improvements across embedding parameters. For the double pendulum, the intrinsic stochasticity curves satisfy $\hat{\mathcal{E}}_{n,k}^*(\theta_i) < \hat{\mathcal{E}}_{n,k}^*(\sin \theta_i)$ over the tested push-forward horizons n , indicating that $\sin \theta_i$ yields a poorer measurement.

Since F_2 suffers geometric degeneracy near $\cos \theta = 0$, it is theoretically worse than the injectivity. Across both experimental and simulated trajectories, and for a range of horizons n , we calculate \mathcal{E}_n^* for all F_{θ_i} and $F_{\sin \theta_i}$ and observe a consistent order $\mathcal{E}_n^*(F_{\theta_i}) < \mathcal{E}_n^*(F_{\sin \theta_i})$, for $i = 1, 2$, with the gap widening as the push-forward step increases.

Measles outbreaks: As the second example, we use measles outbreak data from New York City between 1928 and 1964, which has been shown to exhibit chaotic behavior [41, 46]. We observe that this measles time-series exhibits an intermittent-burst structure: over long intervals, the values of reported cases remain near a low baseline, while rising rapidly during short bursts. This characteristic is similar to the z_3 -direction observation of the Rössler system. Thus, we take a log transformation of this time-series and then calculate the \mathcal{E}_n^* for two time-delay embeddings $\mathcal{E}_n^*(F(x))$ and $\mathcal{E}_n^*(F(\log(1 + x)))$. We observe that after the log transformation, the value of \mathcal{E}^* consistently increases across different time-delay embedding parameters, as expected. All results are shown in the figure 6.

3.6 Downstream task impact

Here, we investigate the impact of time-delay reconstructions that fail to achieve deterministic closure on downstream tasks. We demonstrate that intrinsic stochasticity \mathcal{E}_n^* , serves as a certificate of deterministic closure for time-delay reconstructions, thereby correlating with the performance of downstream tasks. Specifically, a lower \mathcal{E}_n^* indicates a higher probability that the reconstruction forms an injective map (or homeomorphism) within n -steps at a finite resolution k . We evaluate this using two models: the Extended Dynamic Mode Decomposition (EDMD) [49] and the Delay Invariant Measure (DIM) [5]. We observe that raw time-series exhibiting lower $\hat{\mathcal{E}}_{n,k}^*$ yield superior performance in n -step rollout predictions for both models, which validates $\hat{\mathcal{E}}_{n,k}^*$ as an effective signal or measurement function selector when time-delay reconstructions is applied.

Extended Dynamic Mode Decomposition: We first examine how the non-deterministic closure nature of non-injective time-delay reconstructions influences the predictive capability of the EDMD model. The EDMD model is an interpretable framework that approximates the infinite-dimensional Koopman operator by lifting state variables into a dictionary of nonlinear observables; it has been widely employed for the identification of spectral properties [27] and for the prediction and control of complex nonlinear systems [26, 37].

In the case of partial observations, the process first applies time-delay reconstruction to the observed data, then uses EDMD for rollout prediction. In this experiment, we utilise the z_1 -coordinate and z_3 -coordinate projections of the Rössler system as separate raw time-series inputs. Subsequently, we apply EDMD to learn the dynamics in the embedding space and make rollout predictions based on the reconstructed system. In both experiment setups, third-order polynomial features (e.g., $z_1, z_1^2, z_1^3, z_1^2 z_2, \dots$) serve as the nonlinear observables, while ridge regression is employed to approximate the Koopman operator. The EDMD model is trained on a reconstructed trajectory to learn the dynamics, while a separate trajectory generated from a differential initial condition is used for validation. Performance is evaluated on this validation set using full-state predictions over varying rolling-window horizons. The results are presented in figure 7.

Delay Invariant Measure: In the second experiment, we demonstrate the potential of \mathcal{E}_n^* in identifying optimal embeddings to improve the predictive performance of neural networks using the Delay Invariant Measure (DIM). The DIM method for operator learning was proposed by Botvinick et al. [6], grounded in the theorem that if two systems share the same invariant measure on the attractor manifold via time-delay embedding, they are identical up to a topological conjugate almost everywhere (a.e). While this theorem provides a solid foundation for dynamical system identification, it implicitly assumes that the time-delay embedding faithfully recovers the topological properties of the original system. However, this assumption does not always hold in practice. Therefore, we investigate how \mathcal{E}_n^* can guide the selection of embeddings to enhance the learning performance of DIM.

We utilise the z_1 -axis and z_3 -axis coordinate projections as observables for time-delay embedding and evaluate the rollout predictive performance of the DIM models. For model training, we denote the neural network (a three-layer MLP) as T_θ . Let $\Psi_{(y_k, T_\theta)}^{(m)}$ represent the m -dimensional reconstructed system derived from the time-delay vector y_k . Our objective is to optimise the following loss function:

$$\mathcal{L}(\theta) = D(T_\theta \# \hat{\mu}_N, \hat{\mu}_N) + \sum_{k=1}^K D\left(\Psi_{(y_k, T_\theta)}^{(m)} \# \hat{\mu}_N, \hat{\nu}_{y_k}^{(m)}\right), \quad (35)$$

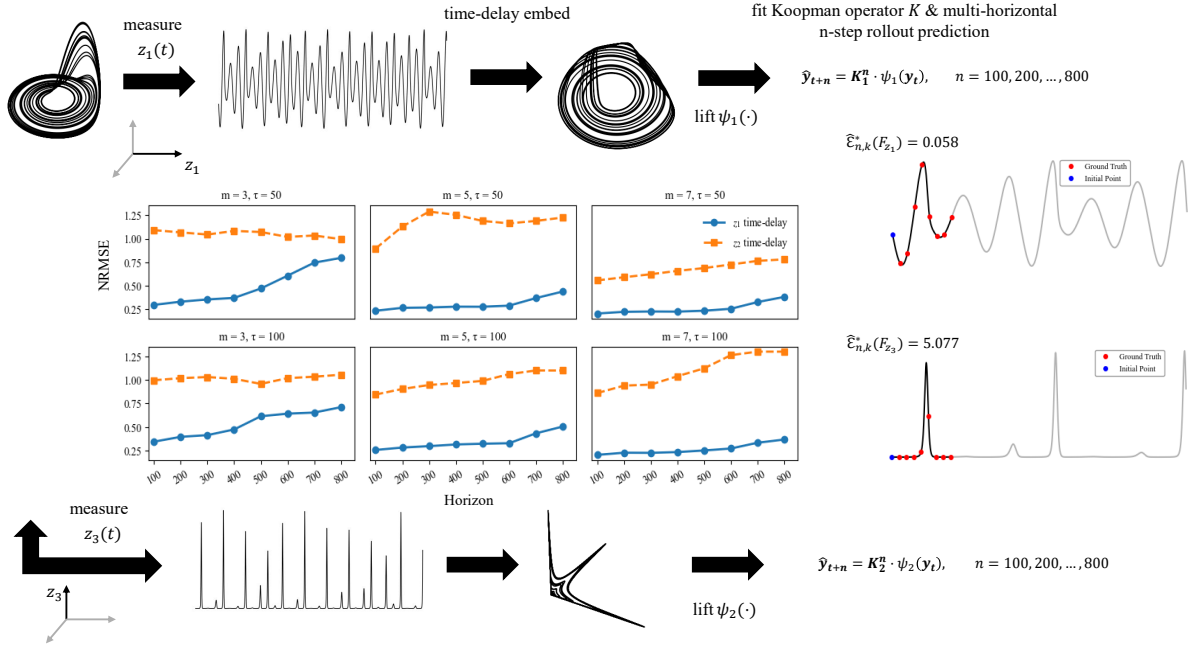


Figure 7: Pipelines for the multi-horizonal rollout prediction using EDMD. We select the z_1 -coordinate and z_3 -coordinate projection of the Rössler system for time-delay reconstruction separately. We then fit the Koopman operators, K_1 and K_2 , on the lifting functions ψ_i , which consist of order-3 polynomials. Subsequently, we use fitted EDMD models to make predictions over multiple horizons with varying embedding parameters and plot the NRMSE ($\sqrt{\text{MSE}}/\sigma$) for both models. Crucially, $\hat{\mathcal{E}}_{n,k}^*(F_{z_1}) < \hat{\mathcal{E}}_{n,k}^*(F_{z_3})$ indicates that the z_1 time-delay works as a superior measurement, aligning with the prediction results.

where $\hat{\mu}_N$ is the kernel density estimation (KDE) of the invariant measure estimated from N samples, and $T_\theta \# \mu_N$ is the corresponding push-forward invariant measure on the Rössler system. D denotes the energy distance. Similarly, $\hat{\nu}_{y_k}^{(m)}$ and $\Psi_{(y_k, T_\theta)}^{(m)} \# \mu_N$ represent the target empirical invariant measure and the predicted push-forward invariant measure on the m -dimensional reconstructed system, respectively. The results are presented in figure 8.

4 Discussion and conclusion

In this paper, we addressed a long-neglected problem in the nonlinear time-series community: quantifying the quality of time-delay reconstructions (e.g., non-injectivity or self-overlap) without any prior information. Despite its ubiquity, time-delay embedding can silently destroy determinism in reconstructed dynamics, leading to irreducible information loss and degeneration of downstream model performance in scientific discovery and prediction. We propose a measure-theoretic framework that lifts the dynamical system from the state space to the space of probability measures by replacing the n -step evolution with the induced n -step kernel $K^n(x, \cdot)$, i.e., the conditional distribution of futures given a reconstructed state. This perspective makes explicit that, when the delay map is non-injective, the statistically correct closure is inherently stochastic rather than a single-valued deterministic map.

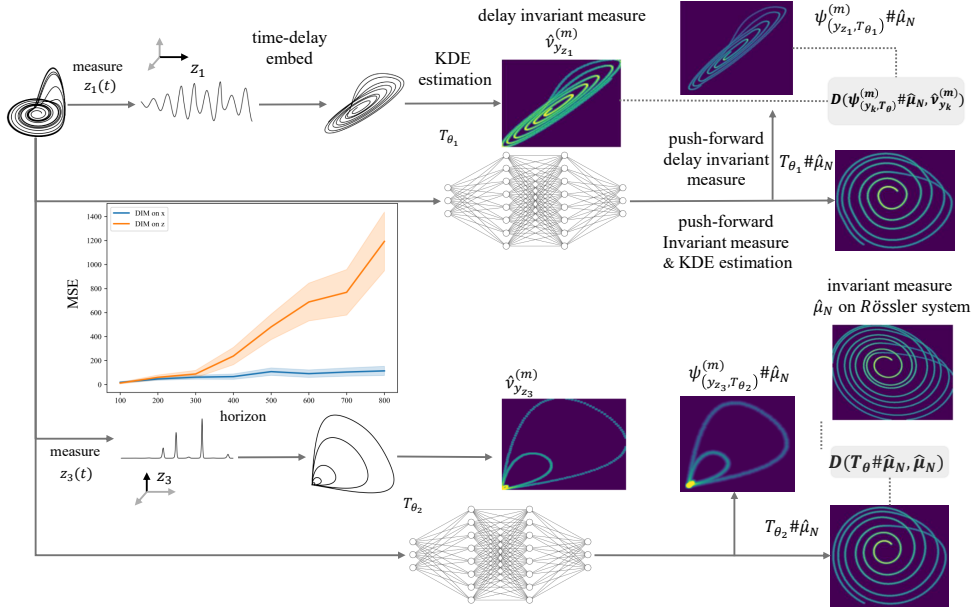


Figure 8: Pipeline for the DIM method. This approach aims to learn the operator/vector field of the dynamical system using a three-layer MLP with 256 hidden units with $\text{Tanh}(x)$ activation function, enforcing the invariant measure of the attractor manifold as a geometric constraint. The Adam optimiser is applied for model training, running for 3000 epochs with a learning rate is $1e - 3$. Aligning with the EDMD case, z_1 -axis and z_3 -axis coordinate projections of the Rössler system are used for time-delay reconstruction, and all measures come out from the KDE estimator. Experimental setups fix the time-delay $\tau = 30$, the embedding dimension $m = 5$, and the push-forward step is 20. For the prediction validation, 30 initial points are randomly chosen from the full state space to perform rollout predictions (within the Lyapunov time). The cumulative MSE on each horizon, along with the 95% confidence interval, is displayed. Notably, $\hat{\mathcal{E}}_{n,k}^*(F_{z_1}) = 0.135$ is smaller than $\hat{\mathcal{E}}_{n,k}^*(F_{z_3}) = 5.79$, which aligns with the model performance.

Inspired by this insight, we introduce an almost-everywhere (a.e) certificate of deterministic closure, the Intrinsic Stochasticity \mathcal{E}_n^* , and explain the geometric mechanism of the generation of self-overlap as well as the information loss. Our numerical experiments on synthetic and real-world datasets support the practical utility of \mathcal{E}_n^* and show that it provides a principled alternative to commonly used heuristics. All code is available at <https://github.com/CrispDyt/Wasserstein-Geometry-of-Information-Loss-in-Nonlinear-Dynamical-Systems>.

Establishing this measure-theoretical framework not only bridges a gap in the theoretical study of non-injective of time-delay reconstructions but also opens the door to a wide range of applications and future work. By clarifying this inevitable information loss, we now better understand the requirements and limitations of time-delay embedding, and our framework has the potential to serve as a measurement selector and to guide the choice of signal transformations that improve downstream performance. For instance, by comparing the Intrinsic Stochasticity, we confirm that the log transformation can substantially improve model performance for intermittent spike-like signals, as illustrated by the NYC measles incidence series. This viewpoint is also provide insights for essential

questions in related field, including control and network science, e.g., how to select informative combinations of observers and how to determine the minimal number of sensors required to reconstruct high-dimensional dynamics without information of governing equations [35, 33, 34, 32]. Our future work focus on the application in these fields and understand the information loss from the perspective of entropy.

A Differential embeddings of Rössler system

In this section, we provide details about the differential mappings of the Rössler system, which serves as the analytic form of the time-delay map we used in Section 3.4. The formulation of Rössler system is:

$$\begin{aligned}\dot{z}_1 &= -z_2 - z_3, \\ \dot{z}_2 &= z_1 + az_2, \\ \dot{z}_3 &= b + z_3(z_1 - c),\end{aligned}\tag{36}$$

with the standard chaotic parameter values $a = 0.2, b = 0.2, c = 5.7$.

Recall the differential mapping (5) defined in Section 2.1, we categorise differential embeddings according to the degeneracy of the singular set in the ambient space (e.g. Euclidean Space \mathbb{R}^3 in our case) of the differential mapping F . Define

$$\Sigma_F := \{\mathbf{z} \in \mathbb{R}^3 : \det DF(\mathbf{z}) = 0\}.\tag{37}$$

We say that F is purely transverse if every point on Σ_F is a simple zero of $\det DF$, i.e.

$$\forall \mathbf{z} \in \Sigma_F : \quad \nabla(\det DF)(\mathbf{z}) \neq 0.\tag{38}$$

We say that F exhibits a degenerate fold if Σ_F contains at least one degenerate point, i.e. if there exists $\mathbf{z} \in \Sigma_F$ such that

$$\nabla(\det DF)(\mathbf{z}) = 0.\tag{39}$$

Finally, we classify F as diffeomorphic on the considered invariant set if Σ_F is not visited or is empty, equivalently $\det DF(\mathbf{z}) \neq 0$ for all \mathbf{z} on that set. In this case, F is locally invertible everywhere on the invariant set with a deterministic closure. However, we emphasise that this classification (diffeomorphic/pure transverse/degenerate fold) in the ambient space characterises local criticality of DF and the associated singularities of an explicitly eliminated vector field; it is not a direct quantitative measure of global non-injectivity/self-overlap of the time-delay reconstruction. For instance, for a given embedding, one may find degenerate points in Σ_F that lie outside or carry negligible SRB mass near the attractor; in that case, the corresponding degeneracy is rarely, if ever, sampled along typical trajectories and has little practical effect. In particular, the impact of Σ_F on time-delay/differential embedding reconstruction depends on the SRB measure on the attractor: only the intersection $\Sigma_F \cap \text{supp}(\nu)$, or more generally the SRB mass of a small neighbourhood of Σ_F , can affect the observed multi-valued evolution.

Univariate differential embedding

For the z_1 -coordinate projection $h(z_1, z_2, z_3) = z_1$ with $m = 3$, the differential map $F_{z_1} : \mathbb{R}^3 \rightarrow \mathbb{R}^3$ is:

$$F_{z_1}(z_1, z_2, z_3) = (u, v, w) = \left(z_1, -z_2 - z_3, -z_1 - az_2 - b - z_3(z_1 - c) \right).\tag{40}$$

On the subset where F_{z_1} is a local diffeomorphism, the induced dynamics in (u, v, w) is single-valued and satisfies $\dot{F}_{z_1} = DF_{z_1} f$. Eliminating (z_1, z_2, z_3) yields the induced vector field $\Psi_{z_1}(u, v, w)$ given by

$$\Psi_{z_1} = \begin{cases} \dot{u} = v, \\ \dot{v} = w, \\ \dot{w} = ab - cu + u^2 - auv + uw + acv + (a - c)w - \frac{(a + c + w - av + b)v}{a + c - u}. \end{cases} \quad (41)$$

This expression is rational and becomes singular on the plane $\mathcal{S}_{z_1} = \{z_1 = a + c\}$, which coincides with the critical set of F_{z_1} (i.e., $\Sigma_F := \{\mathbf{z} \in \mathcal{M} : \det DF_{z_1} = 0\}$). And we can easily get $\nabla(\det DF_{z_1}) = \nabla(z_1 - (a + c)) = (1, 0, 0) \neq 0$, which indicates F_{z_1} belongs to the range of pure transverse. We emphasise, however, that criticality of DF_{z_1} is neither necessary nor sufficient for global non-injectivity/self-overlaps of the reconstruction, which are instead governed by the stretching-curvature competition mechanism we introduced. We next list the three families of differential embeddings used in our experiments.

For the z_2 -coordinate projection $h(z_1, z_2, z_3) = z_2$ with $m = 3$, the differential map $F_{z_2} : \mathbb{R}^3 \rightarrow \mathbb{R}^3$ is:

$$F_{z_2}(z_1, z_2, z_3) = (u, v, w) = (z_2, z_1 + az_2, -z_2 - z_3 + az_1 + a^2 z_2) \quad (42)$$

so that $(z_1, z_2, z_3) \mapsto (u, v, w) = (z_2, \dot{z}_2, \ddot{z}_2)$ defines the z_2 -induced differential embedding. In this case, the Jacobian matrix $J(\Phi_{z_2})$ has determinant

$$\det J(\Phi_{z_2}) \equiv 1. \quad (43)$$

Hence F_{z_2} is a global C^1 diffeomorphism $\mathbb{R}^3 \rightarrow \mathbb{R}^3$ and the associated singular set is empty:

$$\mathcal{S}_{z_2} = \emptyset. \quad (44)$$

In this sense, the F_{z_2} provides a perfect differential embedding of the Rössler flow.

For the z_3 -coordinate projection, the corresponding differential embedding is as follows:

$$F_{z_3}(z_1, z_2, z_3) = (u, v, w) = (z_3, b + z_3(z_1 - c), (b + z_3(z_1 - c))(z_1 - c) + z_3(-z_2 - z_3)). \quad (45)$$

The Jacobian determinant takes the straightforward form

$$\det J(\Phi_{z_3}) = -z_3^2. \quad (46)$$

Hence, the singular set of F_{z_3} is: $\Sigma_{z_3} = \{z_3 = 0\}$, $\nabla(\det DF_{z_3}) = \nabla(-z_3^2) = (0, 0, -2z_3)$, which indicates that on the singular set $\Sigma_{z_3} = z_3 = 0$, we have $\nabla(\det DF) = 0$, thus belonging to degenerate fold.

Differential embedding induced by linear combination of multiple observables

When multiple observations are available, we need to determine how to combine them to improve observability optimally. An intuitive idea is the linearly combine those observations; however, we show that the linear combination may not constantly improve observability due to the complex nonlinear structure of the vector field.

Table 3: Analytic differential mappings and their singular sets for selected multivariate embeddings of the Rössler system. Here $\Sigma_F := \{(z_1, z_2, z_3) : \det DF(z_1, z_2, z_3) = 0\}$.

Embedding	Explicit form	Singular set Σ_F	$\nabla(\det DF)$
(z_1, z_2, \dot{z}_1)	$(z_1, z_2, -z_2 - z_3)$	\emptyset (Diffeomorphism)	$(0, 0, 0)$
(z_1, z_3, \dot{z}_1)	$(z_1, z_3, -z_2 - z_3)$	\emptyset (Diffeomorphism)	$(0, 0, 0)$
(z_2, z_3, \dot{z}_2)	$(z_2, z_3, z_1 + az_2)$	\emptyset (Diffeomorphism)	$(0, 0, 0)$
(z_2, z_3, \dot{z}_3)	$(z_2, z_3, b + z_3(z_1 - c))$	$\{z_3 = 0\}$	$(0, 0, 1)$ (pure transverse)

Observable $z_3' = z_1 + z_2$ For the sum of the z_1 and z_2 variables, the coordinate transformation $F_{z_3'}$ is given by:

$$F_{z_3'} = (u, v, w) = (z_1 + z_2, z_1 + (a-1)z_2 - z_3, (a-1)z_1 + (a^2 - a - 1)z_2 + z_3(c-1-z_1) - b). \quad (47)$$

and the corresponding singular set is:

$$\Sigma_{z_3'} = \{(z_1, z_2, z_3) : (a-2)z_1 + (2c + 3a - ac - a^2 - 2) - z_3 = 0\}. \quad (48)$$

which is a surface parallel to the z_2 -direction. And $\nabla(\det DF_{z_3'}) = (2-a, 0, 1) \neq 0$, which indicates that $F_{z_3'}$ is purely transverse.

Observable $z_2' = z_1 + z_3$ For the observable combining z_1 and z_3 , the differential embedding $F_{z_2'}$ is defined by:

$$\begin{aligned} F_{z_2'} &= (u, v, w) \\ &= (z_1 + z_3, -z_2 - z_3 + b + z_3(z_1 - c), -b(c+1) + (b-1)z_1 - az_2 + c(c+1)z_3 \\ &\quad - (1+2c)z_1z_3 + z_1^2z_3 - z_2z_3 - z_3^2), \end{aligned} \quad (49)$$

which a Jacobian vanishing on the singular set $\Sigma_{F_{z_2'}}$, and $\nabla(\det DF_{z_2'}) = (a+2c+1) + 3z_3 - 2z_1, 1, 3z_1 - (a+3c) - 2z_3) \neq 0$, indicating a pure transverse.

Observable $z_1' = z_2 + z_3$ Finally, we consider mixing the linear component z_2 with the nonlinear component z_3 . The transformation $F_{z_1'}$ involves:

$$\begin{aligned} F_{z_1'} &= (u, v, w) \\ &= (z_2 + z_3, z_1 + az_2 + b + z_3(z_1 - c), -bc + (a+b)z_1 + (a^2 - 1)z_2 + (c^2 - 1)z_3 \\ &\quad - 2cz_1z_3 - z_2z_3 - z_3^2 + z_1^2z_3), \end{aligned} \quad (50)$$

which has the singular set $\Sigma_{z_1'} = \{(z_1, z_2, z_3) : z_2 + z_3^2 + z_3((z_1 - (a+c))^2 + z_2 + 1) + (a+b+2c)z_1 - z_1^2 - (ab+ac+bc+c^2) = 0\}$. Then we can obtain $\nabla(\det DF_{z_1'}) = ((a+b+2c-2z_1) + 2z_3(z_1 - (a+c)), 1 + z_3, (z_1 - (a+c))^2 + z_2 + 2z_3 + 1)$. Letting $z_3 = -1$ and $a = b$, there exists a degeneration point $(z_1, z_2, z_3) = (a+c, 1, -1)$ which satisfies both $\det DF_{z_1'} = 0$ and $\nabla(\det DF_{z_1'}) = 0$, thus admitting a degenerate fold.

Multi-variate differential embedding

Furthermore, we follow the same method and list multi-variate differential embeddings we used in the following table 3.

References

- [1] Luis A Aguirre and Christophe Letellier. Investigating observability properties from data in nonlinear dynamics. *Physical Review E—Statistical, Nonlinear, and Soft Matter Physics*, 83(6):066209, 2011.
- [2] Luis Antonio Aguirre and Christophe Letellier. Observability of multivariate differential embeddings. *Journal of Physics A: Mathematical and General*, 38(28):6311, 2005.
- [3] Luigi Ambrosio, Nicola Gigli, and Giuseppe Savaré. *Gradient flows: in metric spaces and in the space of probability measures*. Springer, 2005.
- [4] Joseph Bakarji, Kathleen Champion, J Nathan Kutz, and Steven L Brunton. Discovering governing equations from partial measurements with deep delay autoencoders. *Proceedings of the Royal Society A*, 479(2276):20230422, 2023.
- [5] Jonah Botvinick-Greenhouse, Robert Martin, and Yunan Yang. Invariant measures in time-delay coordinates for unique dynamical system identification. *Physical Review Letters*, 135(16):167202, 2025.
- [6] Jonah Botvinick-Greenhouse, Maria Oprea, Romit Maulik, and Yunan Yang. Measure-theoretic time-delay embedding. *Journal of Statistical Physics*, 192(12):171, 2025.
- [7] Alex Bradley, Claire Lawrence, and Eamonn Ferguson. Does observability affect prosociality? *Proceedings of the Royal Society B: Biological Sciences*, 285(1875):20180116, 2018.
- [8] David S Broomhead and Gregory P King. Extracting qualitative dynamics from experimental data. *Physica D: Nonlinear Phenomena*, 20(2-3):217–236, 1986.
- [9] Steven L Brunton, Bingni W Brunton, Joshua L Proctor, Eurika Kaiser, and J Nathan Kutz. Chaos as an intermittently forced linear system. *Nature communications*, 8(1):19, 2017.
- [10] Steven L Brunton, Marko Budišić, Eurika Kaiser, and J Nathan Kutz. Modern koopman theory for dynamical systems. *arXiv preprint arXiv:2102.12086*, 2021.
- [11] Steven L Brunton, Joshua L Proctor, and J Nathan Kutz. Discovering governing equations from data by sparse identification of nonlinear dynamical systems. *Proceedings of the national academy of sciences*, 113(15):3932–3937, 2016.
- [12] Kathleen Champion, Bethany Lusch, J Nathan Kutz, and Steven L Brunton. Data-driven discovery of coordinates and governing equations. *Proceedings of the National Academy of Sciences*, 116(45):22445–22451, 2019.
- [13] Daniel J Cross and R Gilmore. Differential embedding of the lorenz attractor. *Physical Review E—Statistical, Nonlinear, and Soft Matter Physics*, 81(6):066220, 2010.
- [14] Siddhasattwa Das and Dimitrios Giannakis. Delay-coordinate maps and the spectra of koopman operators. *Journal of Statistical Physics*, 175(6):1107–1145, 2019.

- [15] Yiting Duan, Yi Guo, Jack Yang, and Ming Yin. Causal discovery in symmetric dynamic systems with convergent cross mapping. *arXiv preprint arXiv:2505.04815*, 2025.
- [16] J-P Eckmann and David Ruelle. Ergodic theory of chaos and strange attractors. *Reviews of modern physics*, 57(3):617, 1985.
- [17] Bingbo Gao, Jianyu Yang, Ziyue Chen, George Sugihara, Manchun Li, Alfred Stein, Mei-Po Kwan, and Jinfeng Wang. Causal inference from cross-sectional earth system data with geographical convergent cross mapping. *nature communications*, 14(1):5875, 2023.
- [18] Dimitrios Giannakis. Delay-coordinate maps, coherence, and approximate spectra of evolution operators. *Research in the Mathematical Sciences*, 8(1):8, 2021.
- [19] Christopher E Gonzalez, Claudia Lainscsek, Terrence J Sejnowski, and Christophe Letellier. Assessing observability of chaotic systems using delay differential analysis. *Chaos: An Interdisciplinary Journal of Nonlinear Science*, 30(10), 2020.
- [20] James D Hamilton. *Time series analysis*. Princeton university press, 2020.
- [21] Robert Hermann and Arthur Krener. Nonlinear controllability and observability. *IEEE Transactions on automatic control*, 22(5):728–740, 2003.
- [22] Seth M Hirsh, Sara M Ichinaga, Steven L Brunton, J Nathan Kutz, and Bingni W Brunton. Structured time-delay models for dynamical systems with connections to frenet–serret frame. *Proceedings of the Royal Society A*, 477(2254):20210097, 2021.
- [23] Kadierdan Kaheman, Eurika Kaiser, Benjamin Strom, J Nathan Kutz, and Steven L Brunton. Learning discrepancy models from experimental data. *arXiv preprint arXiv:1909.08574*, 2019.
- [24] Mason Kamb, Eurika Kaiser, Steven L Brunton, and J Nathan Kutz. Time-delay observables for koopman: Theory and applications. *SIAM Journal on Applied Dynamical Systems*, 19(2):886–917, 2020.
- [25] Matthew B Kennel, Reggie Brown, and Henry DI Abarbanel. Determining embedding dimension for phase-space reconstruction using a geometrical construction. *Physical review A*, 45(6):3403, 1992.
- [26] Stefan Klus, Frank Nüsken, Péter Koltai, Hao Wu, Ioannis G Kevrekidis, and Christof Schütte. Data-driven approximation of the koopman generator: Model reduction, system identification, and control. *Physica D: Nonlinear Phenomena*, 406:132416, 2020.
- [27] Milan Korda and Igor Mezić. Linear predictors for nonlinear dynamical systems: Global stability and control. *Automatica*, 93:149–160, 2018.
- [28] J Nathan Kutz and Steven L Brunton. Parsimony as the ultimate regularizer for physics-informed machine learning. *Nonlinear Dynamics*, 107(3):1801–1817, 2022.
- [29] Claudia Lainscsek, Christophe Letellier, and Irina Gorodnitsky. Global modeling of the rössler system from the z-variable. *Physics Letters A*, 314(5-6):409–427, 2003.

- [30] Christophe Letellier and Luis A Aguirre. Investigating nonlinear dynamics from time series: The influence of symmetries and the choice of observables. *Chaos: An Interdisciplinary Journal of Nonlinear Science*, 12(3):549–558, 2002.
- [31] Christophe Letellier, Luis A Aguirre, and Jean Maquet. Relation between observability and differential embeddings for nonlinear dynamics. *Physical Review E—Statistical, Nonlinear, and Soft Matter Physics*, 71(6):066213, 2005.
- [32] Christophe Letellier, Irene Sendiña-Nadal, Ezequiel Bianco-Martinez, and Murilo S Baptista. A symbolic network-based nonlinear theory for dynamical systems observability. *Scientific reports*, 8(1):3785, 2018.
- [33] Yang-Yu Liu and Albert-László Barabási. Control principles of complex systems. *Reviews of Modern Physics*, 88(3):035006, 2016.
- [34] Yang-Yu Liu, Jean-Jacques Slotine, and Albert-László Barabási. Controllability of complex networks. *nature*, 473(7346):167–173, 2011.
- [35] Yang-Yu Liu, Jean-Jacques Slotine, and Albert-László Barabási. Observability of complex systems. *Proceedings of the National Academy of Sciences*, 110(7):2460–2465, 2013.
- [36] Wayne P London and James A Yorke. Recurrent outbreaks of measles, chickenpox and mumps: I. seasonal variation in contact rates. *American journal of epidemiology*, 98(6):453–468, 1973.
- [37] Bethany Lusch, J Nathan Kutz, and Steven L Brunton. Deep learning for universal linear embeddings of nonlinear dynamics. *Nature Communications*, 9(1):4950, 2018.
- [38] Norman H Packard, James P Crutchfield, J Doyne Farmer, and Robert S Shaw. Geometry from a time series. *Physical review letters*, 45(9):712, 1980.
- [39] J-C Roux, Reuben H Simoyi, and Harry L Swinney. Observation of a strange attractor. *Physica D: Nonlinear Phenomena*, 8(1-2):257–266, 1983.
- [40] Tim Sauer, James A Yorke, and Martin Casdagli. Embedology. *Journal of statistical Physics*, 65(3):579–616, 1991.
- [41] William M Schaffer and Mark Kot. Do strange attractors govern ecological systems? *BioScience*, 35(6):342–350, 1985.
- [42] Jaroslav Stark. Delay embeddings for forced systems. I. deterministic forcing. *Journal of Nonlinear Science*, 9(3):255–332, 1999.
- [43] Jaroslav Stark, David S. Broomhead, Mark E. Davies, and John Huke. Delay embeddings for forced systems. II. stochastic forcing. *Journal of Nonlinear Science*, 13(6):519–577, 2003.
- [44] Charles J Stone. Consistent nonparametric regression. *The annals of statistics*, pages 595–620, 1977.
- [45] George Sugihara, Robert May, Hao Ye, Chih-hao Hsieh, Ethan Deyle, Michael Fogarty, and Stephan Munch. Detecting causality in complex ecosystems. *science*, 338(6106):496–500, 2012.

- [46] George Sugihara and Robert M May. Nonlinear forecasting as a way of distinguishing chaos from measurement error in time series. *Nature*, 344(6268):734–741, 1990.
- [47] Floris Takens. Detecting strange attractors in turbulence. In *Dynamical Systems and Turbulence, Warwick 1980: proceedings of a symposium held at the University of Warwick 1979/80*, pages 366–381. Springer, 2006.
- [48] James Theiler. Spurious dimension from correlation algorithms applied to limited time-series data. *Physical review A*, 34(3):2427, 1986.
- [49] Matthew O Williams, Ioannis G Kevrekidis, and Clarence W Rowley. A data-driven approximation of the koopman operator: Extending dynamic mode decomposition. *Journal of Nonlinear Science*, 25(6):1307–1346, 2015.
- [50] Yunan Yang, Levon Nurbekyan, Elisa Negrini, Robert Martin, and Mirjeta Pasha. Optimal transport for parameter identification of chaotic dynamics via invariant measures. *SIAM Journal on Applied Dynamical Systems*, 22(1):269–310, 2023.
- [51] Hao Ye, Ethan R Deyle, Luis J Gilarranz, and George Sugihara. Distinguishing time-delayed causal interactions using convergent cross mapping. *Scientific reports*, 5(1):14750, 2015.